

Bulk Photovoltaic Effects in Helimagnets

Chunmei Zhang¹, Jian Zhou^{2,*}

¹School of Physics, Northwest University, Xi'an 710127, China

²Center for Alloy Innovation and Design, State Key Laboratory for Mechanical Behavior of Materials, Xi'an Jiaotong University, Xi'an 710049, China

*Email: jianzhou@xjtu.edu.cn

Abstract

The bulk photovoltaic (BPV) effect that converts light into electric current is highly sensitive to the system symmetry and its electronic Bloch wavefunction. To create a sizable net electric current, it is necessary to break the centrosymmetry \mathcal{P} in its host material. Here, we investigate how helical spin polarization breaks \mathcal{P} that is otherwise kept in its crystalline geometry. The magnetic helix widely exists in multiferroics and magnon excitation in collinear magnets. We apply symmetry analysis and a tight-binding model to show how the symmetry is reduced in helimagnetic platforms under various degrees of freedom, namely, different types of spin spiral configurations, spin winding angles, magnetic propagation vectors, and spin chirality. They offer effective and versatile manipulation of BPV generation in helimagnets. Our concept is further illustrated in the monolayer NiI_2 , a typical helimagnetic material. It could host observable direction-dependent BPV current, which serves as an opto-electric probe to track the subtle magnetic configurations and potential ferroic nature. Our work reveals the fundamental mechanism of the multiferroic order and the nonlinear optics process.

Bulk photovoltaic (BPV) effect, a second order nonlinear optical response, could produce a steady state electric current in a single material under homogeneous optical illumination [1-4], which would avoid the complexity of making heterojunctions and engineering defects in conventional photoelectric conversion processes. Up to now, the underlying mechanisms of BPV generation have been enumerated into two main categories, namely, the shift current and injection current, depending on the light polarization and the specific material symmetry. As the light alternating field does not break centrosymmetry (\mathcal{P}), both BPV processes only emerge in systems without \mathcal{P} . Hence, most hitherto studies are limited to polar materials, especially ferroelectrics.

Recently, attention has been paid to antiferromagnetic materials with a combined \mathcal{PT} symmetry [5-12], where \mathcal{T} refers to time-reversal symmetry. In these materials, it has been shown that the magnetic counterparts of shift and injection current would arise, due to the inequivalent distribution of the Kramers pair states at \mathbf{k} and $-\mathbf{k}$. This results in a total of four different BPV currents in intrinsic semiconductors, which are all rooted in topological phases of Bloch electronic wavefunctions, namely, shift vectors, Berry curvature, and quantum metrics [13-15]. In this Letter, we investigate a more general case that gives rise to BPV current in crystalline centrosymmetric materials under spin spiral configurations. The collective spin spiral pattern, which usually appears under magnon excitation or multiferroic materials, offers ultrafast dynamics and low energy dissipation in information storage and manipulation [16]. Until now, rare studies have been performed to focus on the interplay between the helical spin and the BPV effect.

We scrutinize how the spin spiral pattern manipulates observable BPV currents with controllable directions. Two typical helimagnetic states, namely, cycloid and proper screw configurations, are used to illustrate our theory. They refer to the helical spin plane parallel and perpendicular to the magnetic propagation vector \mathbf{q} , respectively. It has been shown that the spin helix induces electric polarization according to $\mathbf{P}_{ij} = A\mathbf{e}_{ij} \times (\mathbf{S}_i \times \mathbf{S}_j) + B[(\mathbf{e}_{ij} \cdot \mathbf{S}_i)\mathbf{S}_i - (\mathbf{e}_{ij} \cdot \mathbf{S}_j)\mathbf{S}_j]$, where A and B are the coupling parameters arising from spin-orbit coupling (SOC), and \mathbf{e}_{ij} is a unit vector pointing from spin sites \mathbf{S}_j to \mathbf{S}_i . The first term corresponds to the cycloidal spin pattern from the inverse Dzyaloshinskii-Moriya interaction, and the second term gives rise to the polarization in the proper screw spin texture [17]. Hence, the helimagnetic structure could host finite electric polarizations that are strongly coupled to their spin texture, giving a type-II multiferroic character. By performing a simple tight-binding model and a thorough symmetry analysis in the magnetic group theory, we show that they both could generate BPV current, with their flowing directions determined by the specific spin configuration, \mathbf{q} , and the winding angle at the home cell. We further use a realistic material, namely, monolayer NiI_2 , to illustrate this concept by performing first-principles calculations. Note that the monolayer NiI_2 belongs to the transition metal di-iodide ($X\text{I}_2$, $X = \text{Ni, Co, Mn}$) family. In

experiments, their monolayer and bulk phases have been revealed to be helimagnetic [17-22]. In particular, the monolayer NiI_2 is under tremendous experimental and theoretical investigations on its potential multiferroic nature. We suggest that its BPV photoconductance could reach $\sim 50 \mu\text{A}/\text{V}^2$, and the current direction strongly depends on the spin spiral configurations.

We denote a magnetic propagation vector \mathbf{q} to describe the helimagnetic pattern. In general, the local magnetic moment takes the form

$$\mathbf{M}_i = M(\cos \varphi_i \sin \theta_i, \sin \varphi_i \sin \theta_i, \cos \theta_i) \quad (1)$$

Here, θ_i is the polar angle and φ_i is the azimuthal angle of the local magnetic polarization vector at magnetic site i . M is the magnetic exchange value. The proper screw helimagnetic configuration [Fig. 1(a)] is

$$\varphi_i = \frac{\pi}{2}, \theta_i = \theta_0 + \mathbf{q} \cdot \mathbf{r}_i, \quad (2)$$

and the cycloid pattern [Fig. 1(b)] gives

$$\theta_i = \frac{\pi}{2}, \varphi_i = \varphi_0 + \mathbf{q} \cdot \mathbf{r}_i, \quad (3)$$

Here, \mathbf{r}_i is the position of the magnetic site with respect to lattice vectors, and φ_0 and θ_0 are winding angles at the home site ($\mathbf{r}_i = \mathbf{0}$). We denote that (φ, θ) is the same as $(\varphi + \pi, 2\pi - \theta)$, so that the azimuthal angle can be extended in the range of $[0, 2\pi)$, which does not affect the evaluation in Eq. (1).

For simplicity, we assume that each unit cell conceives one magnetic site. The $\mathbf{q} = (q_1, q_2, q_3)$ is measured with respect to reciprocal lattice of the unit cell. For each index j ($j = 1, 2, 3$), $q_j = 0$ refers to ferromagnetic pattern, and $q_j = \pm \frac{1}{2}$ describes the collinear antiferromagnetic configuration. Any nonzero values in the range of $(-\frac{1}{2}, +\frac{1}{2})$ indicate a spiral magnetization structure. We can apply a simple group theory to analyze the parity broken in helimagnetic systems. Note that in order to discuss the interplay between spin and lattice, one has to take the magnetic group theory rather than the spin group theory to conduct the analysis. We begin with a crystalline point group \mathcal{G} that contains \mathcal{P} ($\mathcal{P} \in \mathcal{G}$). Both the trivial magnetic point groups, colorless and gray groups, would then contain \mathcal{P} , so that they generate zero net BPV current. Hence, we focus on the nontrivial black-white magnetic point group, denoted as $\mathcal{G}_m = \mathcal{H} + (\mathcal{G}_0 - \mathcal{H})\mathcal{T}$, where \mathcal{G}_0 is a subgroup of \mathcal{G} and \mathcal{H} is the index-two subgroup of \mathcal{G}_0 , generated by a unitary operation \mathcal{R} . One can also write $\mathcal{G}_m = \mathcal{H} + \mathcal{R}\mathcal{T}$. In the ferromagnetic configuration, $\mathcal{P} \in \mathcal{H}$ since the magnetization transforms as axial vectors. The collinear antiferromagnetic configuration could be either \mathcal{P} or $\mathcal{P}\mathcal{T}$, depending on how to select \mathcal{H} . In

these two cases, one always has $\mathcal{P} \in \mathcal{G}_0$. On the contrary, in the general helimagnetic pattern, one has $\mathcal{P} \notin \mathcal{G}_0$, so that the centrosymmetry is broken, giving finite BPV conductance. We will briefly discuss this case in the following.

Table I. Spin transformation under time reversal, reflection, and 180° rotation operations. Note that here we do not include the crystalline position operations.

Operations	T	\mathcal{M}_x (or $\mathcal{C}_{2x}\mathcal{T}$)	$\mathcal{M}_x\mathcal{T}$ (or $\mathcal{C}_{2x}\mathcal{T}$)	\mathcal{M}_y (or $\mathcal{C}_{2y}\mathcal{T}$)	$\mathcal{M}_y\mathcal{T}$ (or $\mathcal{C}_{2y}\mathcal{T}$)	\mathcal{M}_z (or $\mathcal{C}_{2z}\mathcal{T}$)	$\mathcal{M}_z\mathcal{T}$ (or $\mathcal{C}_{2z}\mathcal{T}$)
(φ, θ)	$\begin{pmatrix} \pi + \varphi \\ \pi - \theta \end{pmatrix}$	$(-\varphi, \pi - \theta)$	$\begin{pmatrix} \pi - \varphi \\ \theta \end{pmatrix}$	$\begin{pmatrix} \pi - \varphi \\ \pi - \theta \end{pmatrix}$	$(-\varphi, \theta)$	$(\pi + \varphi, \theta)$	$\begin{pmatrix} \varphi \\ \pi - \theta \end{pmatrix}$

We take a minimum model to explicitly describe the symmetry broken procedure in a 2D trigonal lattice [Figs. 1(a) and 1(b)]. Regardless the spin helix, its crystalline layer group is $P6/mmm$, corresponding to $\mathcal{G} = D_{6h}$. The helimagnetic vector is taken as $\mathbf{q} = \left(\frac{1}{2}, \frac{1}{4}\right)$ with respect to the reciprocal lattice vectors. It corresponds to collinear antiferromagnetic pattern along \mathbf{a}_1 , and a spiral structure along \mathbf{a}_2 . We then briefly analyze the symmetry operations by focusing on mirror reflection and 180° rotation, which mainly determines the BPV component existence. Table I (and Table S1 in the Supplemental Material [23], which includes references [7] [24-33]) list the transformation of magnetization in the spherical coordinate. In the proper screw state, it always has $\varphi = \frac{\pi}{2}$. As for the polar angle, there is always $\mathcal{C}_{2x}\mathcal{T}$ for any θ_0 , giving a magnetic point group of $2'$. For the cycloid helimagnetic state, the system belongs to $m'm'2 = \mathcal{C}_2 + (\mathcal{C}_{2v} - \mathcal{C}_2)\mathcal{T}$ for $\varphi_0 = 0$. At a general φ_0 , only $\mathcal{M}_z\mathcal{T}$ survives, giving a magnetic point group m' . As such, in helimagnetic situations, the parity \mathcal{P} will break, giving a nonzero BPV effect (except for a few θ_0 or φ_0 cases, as discussed below).

To explicitly illustrate the BPV generation, we construct a tight-binding model to perform the calculation. Without loss of generality, the basis spinor functions are chosen to be $[d_{xy}^\dagger, d_{x^2-y^2}^\dagger, d_{z^2}^\dagger, d_{xy}^\dagger, d_{x^2-y^2}^\dagger, d_{z^2}^\dagger]$. The Hamiltonian reads

$$\hat{H} = \sum_{i,\mu} c_{i\mu,\alpha}^\dagger (\boldsymbol{\sigma} \cdot \mathbf{M}_i)_{\alpha\beta} c_{i\mu,\beta} + \sum_{\langle i,j \rangle, \mu\nu, \alpha} t_{i\mu,j\nu} c_{i\mu,\alpha}^\dagger c_{j\nu,\alpha} + \sum_{i,\mu,\alpha} U_\mu c_{i\mu,\alpha}^\dagger c_{i\mu,\alpha}, \quad (4)$$

where $c_{i,\mu}^\dagger$ ($c_{i,\mu}$) is the creation (annihilation) operator for orbital μ at site i . $\boldsymbol{\sigma}$ are Pauli matrices for spin degree of freedom, characterizing the helical spin pattern. $t_{i\mu,j\nu}$ denotes the hopping integral, which can be expressed by the d - d interactions ($V_{dd\sigma}$, $V_{dd\pi}$, and $V_{dd\delta}$) according to the Slater-Koster scheme. U_μ is the orbital on-site energy, denoting the chemical potential difference between the d_{z^2} and the $(d_{xy}, d_{x^2-y^2})$. We also include on-site intrinsic SOC between the d_{xy} and $d_{x^2-y^2}$ in the same

spin channel, $\hat{H}_{\text{SOC}} = t_{\text{SOC}}\sigma_z h$, with t_{SOC} representing the SOC strength and $h = \begin{pmatrix} 0 & -2i & 0 \\ 2i & 0 & 0 \\ 0 & 0 & 0 \end{pmatrix}$.

The calculated band dispersions are shown in Figs. 1(c) and 1(d). In the proper screw configuration, we take a general initial polar angle of $\theta_0 = \frac{\pi}{18}$ (as $\theta_0 = 0$ is highly symmetric, forbidden BPV generation), and the $\mathcal{C}_{2x}\mathcal{T}$ constraints its electric polarization \mathbf{P} to be along x . For the cycloid pattern, we use $\varphi_0 = 0$, giving \mathbf{P} lies along y . One notes that reversing the spiral chirality (from \mathbf{q} to $-\mathbf{q}$) would flip the electric polarization \mathbf{P} to $-\mathbf{P}$. We choose the Fermi level in between the d_{z^2} and the $(d_{xy}, d_{x^2-y^2})$, leaving semiconducting characters for both cases with bandgaps of 0.3 eV (proper screw) and 0.5 eV (cycloid).

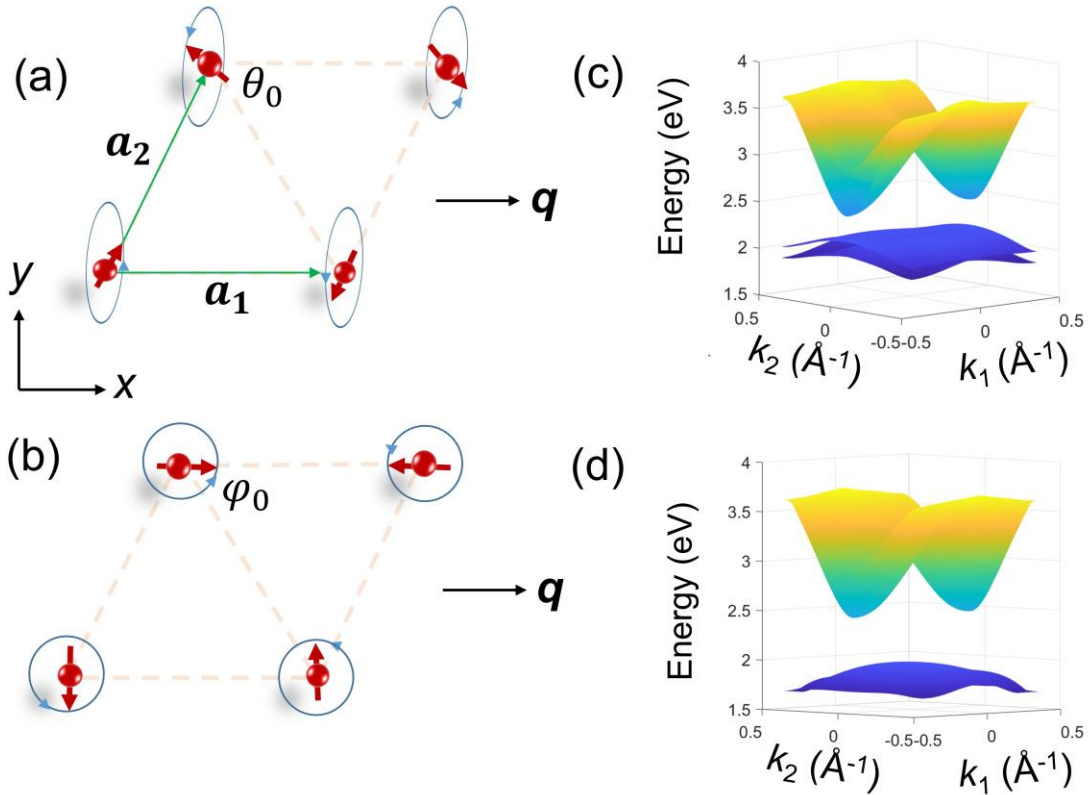


FIG. 1. Schematic plot of the helimagnetic states for the (a) proper screw and (b) cycloid spin spiral order in a 2D trigonal lattice, with $\mathbf{q} = \left(\frac{1}{2}, \frac{1}{4}\right)$. The trigonal lattice constant is chosen to be 4 \AA . Their tight-binding band dispersion in the reciprocal space is plotted in (c) with $\theta_0 = \frac{\pi}{18}$ and (d) with $\varphi_0 = 0$, respectively. The hopping parameters are $V_{dd\sigma} = -0.4$, $V_{dd\pi} = 0.3$, and $V_{dd\delta} = 0.6$. The on-site U values for d_{xy} , $d_{x^2-y^2}$, and d_{z^2} are set to be 0, 0, and 1, respectively. The universal magnetic exchange parameter is $M = 0.7$. The SOC parameter is $t_{\text{soc}} = 0.7$. All of them are in unit of eV.

We now move to the second order BPV generation. We take the linearly polarized light (LPL) irradiation to conduct the analysis. Previous works have shown that LPL could generate two types of photocurrent, namely, the normal shift current (NSC) and the magnetic injection current (MIC) [13],

$$J_{\text{NSC}}^a = \sigma^{abb}(0; \omega, -\omega) E_b(\omega) E_b(-\omega), \quad (5)$$

$$J_{\text{MIC}}^a = \eta^{abb}(0; \omega, -\omega) E_b(\omega) E_b(-\omega). \quad (6)$$

Here, the σ^{abb} and η^{abb} are the photoconductivity for NSC and MIC respectively. E is the light alternating electric field (with angular frequency ω), and a (b) refers to Cartesian coordinate in the xy plane. The NSC is irrespective to \mathcal{T} , which reflects the wavefunction center shift when photon excites the electron from its valence to conduction bands. According to Kubo perturbation theory, its length gauge expression can be evaluated by

$$\sigma^{abb}(0; \omega, -\omega) = \frac{\pi e^3}{\hbar^2} \int \frac{d^3 k}{(2\pi)^3} \sum_{m,n} f_{mn} R_{mn}^{a;b} |r_{mn}^b|^2 \delta(\omega_{mn} - \omega), \quad (7)$$

where f_{mn} and $\hbar\omega_{mn}$ measure the occupation and eigenenergy differences between m and n states, respectively. The interband position operator $r_{mn}^b = \frac{\langle m|v^b|n\rangle}{i\omega_{mn}}$ for $m \neq n$ (v^b is the velocity operator).

The gauge-invariant shift vector is $R_{mn}^{a;b} = \partial_a \phi_{mn}^b - \mathcal{A}_{mm}^a + \mathcal{A}_{nn}^a$, with ϕ_{mn}^b being the phase of r_{mn}^b ($= |r_{mn}^b| e^{i\phi_{mn}^b}$) and $\mathcal{A}_{mm}^a = i\langle m|\partial_a m\rangle$ the intraband Berry connection. Hence, the NSC evaluates the contribution of the shift vector weighted by absorption rate $|r_{mn}^b|^2 \delta(\omega_{mn} - \omega)$ at each \mathbf{k} . All these quantities are \mathbf{k} -dependent, which is omitted for clarity reason.

The \mathcal{T} -odd MIC characterizes the band velocity differences between the valence and conduction bands, taking the form,

$$\eta^{abb}(0; \omega, -\omega) = -\frac{\tau\pi e^3}{\hbar^2} \int \frac{d^3 k}{(2\pi)^3} f_{mn} \Delta_{mn}^a g_{mn}^{bb} \delta(\omega_{mn} - \omega). \quad (8)$$

Here, $\Delta_{mn}^a = v_{mm}^a - v_{nn}^a$ denotes the velocity difference and the quantum metric tensor $g_{mn}^{bb} = |r_{mn}^b|^2$ is the real and symmetric part of the electronic Bloch wavefunction. The MIC linearly grows with time and saturates at carrier relaxation time τ , which is multiplied as a pre-factor in Eq. (8).

Since the helimagnetic configuration is in neither \mathcal{P} nor \mathcal{PT} , both NSC and MIC may emerge. For the proper screw pattern, we have $\mathcal{C}_{2x}\mathcal{T}R_{mn}^{y;b}(k_x, k_y) = -R_{mn}^{y;b}(-k_x, k_y)$ ($b = x, y$, representing LPL polarization direction along principal axis). Hence, one always has σ^{yyy} and σ^{yxx} symmetrically forbidden, leaving only σ^{xxx} and σ^{xyy} to be finite. As the \mathcal{C}_{3z} is broken under the helimagnetic pattern, these two components are independent of each other. This demonstrates that the NSC is unidirectional under proper screw configuration. One notes that this trigonal lattice cannot host NSC generation under nonmagnetic, ferromagnetic, or collinear antiferromagnetic configurations. It is the helimagnetic pattern that breaks \mathcal{P} . Our tight-binding calculations show consistent results [Fig. 2(a)]. For the cycloid pattern, its x -propagation current will be forbidden as $\mathcal{C}_{2y}R_{nm}^{x;b}(k_x, k_y) = -R_{nm}^{x;b}(-k_x, k_y)$, so that the NSC is also unidirectional and only transports along y , as numerically calculated in Fig. 2(b).

Similar symmetric analysis can be conducted for the MIC generation. For the proper screw pattern, one has $\mathcal{C}_{2x}\mathcal{T}\Delta^x(k_x, k_y) = -\Delta^x(-k_x, k_y)$ [34]. The quantum metric remains intact as $\mathcal{C}_{2x}\mathcal{T}g_{nm}^{bb}(k_x, k_y) = g_{nm}^{bb}(-k_x, k_y)$. Therefore, under (x or y -polarized) LPL, the MIC in proper screw helimagnets only transports along y . The results are plotted in Fig. S1 [23]. This is normal to the NSC flowing direction, so that they can be individually measured experimentally. Compared with NSC, our results reveal that the MIC is much weaker (when we take a conservative and experimentally achievable τ on the order of 0.1 ps). Nonetheless, the MIC and NSC generation can be distinguished by comparing their τ -dependence. For the cycloid pattern, one can show that the MIC generation is always forbidden, under the m' magnetic point group. This can be understood by the isomorphic group theory. The b -LPL transforms as A' in the C_s point group, the \mathcal{T} and the in-plane current follow the A'' irreducible representation. Hence, the in-plane MIC generation follows $A' \otimes A'' \otimes A' = A''$, which is forbidden in symmetry. Alternatively, under $\mathcal{M}_z\mathcal{T}$, one has $\mathcal{M}_z\mathcal{T}\Delta^b(k_x, k_y) = -\Delta^b(-k_x, -k_y)$ and $\mathcal{M}_z\mathcal{T}g_{nm}^{bb}(k_x, k_y) = g_{nm}^{bb}(-k_x, k_y)$. Thus, it gives a zero MIC when conducting integration in the whole first Brillouin zone (BZ).

We would like to point out that there are additional symmetry correspondences for the home winding angles and \mathbf{q} values. Taking NSC generation in the proper screw helimagnetic state as an example. We find that when $\theta_0 = \nu' \frac{\pi}{4}$ ($\nu' \in \mathbb{Z}$), the system possesses \mathcal{C}_{2y} or \mathcal{C}_{2z} (or their multiplications with \mathcal{T}), besides the existing $\mathcal{C}_{2x}\mathcal{T}$. For example, at $\theta_0 = 0$, we have additional $\mathcal{C}_{2y}\mathcal{T}$ and \mathcal{C}_{2z} , giving a magnetic point group of $2'2'2 = C_2 + (D_2 - C_2)\mathcal{T}$. Then the NSC is forbidden when the irradiating LPL is polarized along x or y . A general and detailed derivation can be found in Supplemental Material and Fig. S2 [23], which shows that the NSC would diminish at $\theta_0 = \frac{\nu' \pi}{2\ell}$ for $\mathbf{q} = \left(\frac{1}{\ell}, \frac{1}{2\ell}\right)$. For the $\mathbf{q} = \left(\frac{1}{2}, \frac{1}{4}\right)$ case, these angles are $\theta_0 = 0, \pm\frac{\pi}{4}, \pm\frac{\pi}{2}, \pm\frac{3\pi}{4} \dots$ (following the C_2 point group), and $\sigma_{\text{prop}}^{xbb}$ varies periodically with θ_0 as shown in Fig. S3 [23]. If we reverse the spin chirality, $\mathbf{q} \rightarrow -\mathbf{q}$, the NSC photoconductance flips its propagating direction, as shown in Fig. S4 [23]. For another \mathbf{q} value, note that the symmetry arguments would alter. To illustrate this, we plot the results for $\mathbf{q} = \left(\frac{1}{4}, \frac{1}{8}\right)$ in Figs. S5 and S6 [23].

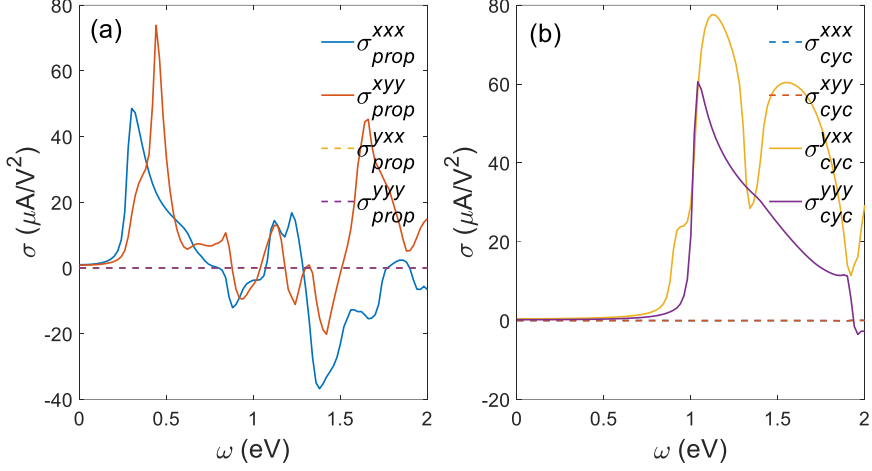


FIG. 2. The tight-binding model based NSC photoconductance for $\mathbf{q} = \left(\frac{1}{2}, \frac{1}{4}\right)$ in (a) the proper screw ($\theta_0 = \frac{\pi}{18}$) and (b) the cycloid ($\varphi_0 = 0$) helimagnetic configurations. The dashed lines are symmetrically forbidden components. The abscissa axis denotes incident photon energy. We assume an artificial layer thickness of 0.5 Å, so that the photoconductance unit is in accordance with conventional 3D systems.

With the magnetic symmetry and BPV generation (under LPL) analyzed in the toy model, we carry out first-principles density functional theory (DFT) calculations in a realistic helimagnetic material, monolayer NiI_2 . The computational details can be found in Supplemental Material [23]. As plotted in Fig. 3(a), the Ni sites show a trigonal lattice, and the iodine atoms form two atomic layers, giving a 1T phase [35]. It exhibits a crystalline layer group of $P\bar{3}m1$. Experimentally, the monolayer NiI_2 can be exfoliated from its bulk counterpart and is characterized in the proper screw and cycloidal spin helix, depending on its substrates [36-39]. This material has been receiving tremendous attention due to its unique helical spin order and its multiferroic order is still under extensive investigation [17,40-43].

According to previous works, the monolayer NiI_2 prefers a $\mathbf{q} = \left(\frac{1}{4}, \frac{1}{8}\right)$ [19,44,45], and we will be focusing on this pattern [Fig. 3(e)]. Our DFT calculations suggest that the proper screw (with $\theta_0 = 0$) [Fig. 3(b)] is energetically lower than the cycloid spiral state ($\varphi_0 = 0$) [Fig. 3(c)] by 3 meV (per unit cell). No matter which specific pattern is chosen, the calculated bandgap is ~ 0.9 eV. We calculate their electric polarization, giving $\mathbf{P} = (-2.85 \times 10^{-12}, 0, 0)$ C/m for the proper screw pattern, and $\mathbf{P} = (0, -9.67 \times 10^{-13}, 0)$ C/m for the cycloid configuration. All these results agree well with the symmetry consideration and previous results [36,39].

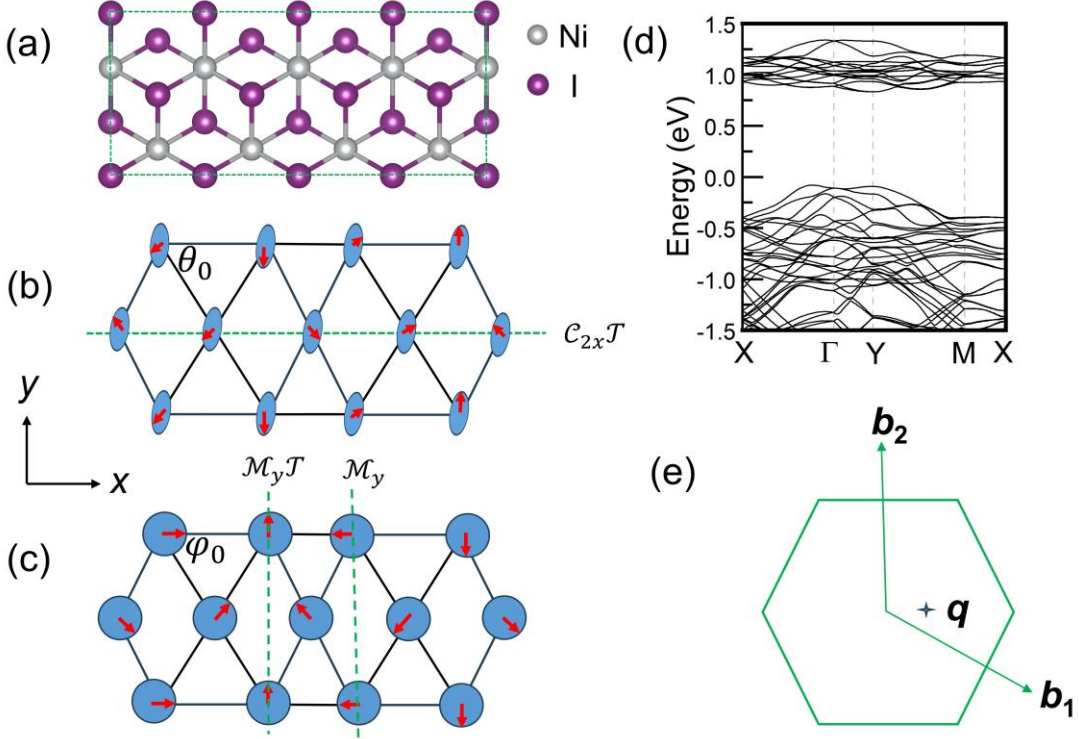


FIG. 3. (a) Ball and stick plot of the top view of monolayer NiI_2 , and the dashed rectangle denotes simulation supercell. Note that here the 1T crystalline structure is quasi-2D, lower in symmetry than the strict 2D trigonal lattice. Schematic plot of (b) proper screw and (c) cycloid configurations. (d) Band dispersion calculated in the proper screw spin pattern with $\mathbf{q} = \left(\frac{1}{4}, \frac{1}{8}\right)$. (e) The first BZ of trigonal lattice and the position of \mathbf{q} in the reciprocal space.

We plot the DFT calculated NSC and MIC photoconductance for both proper screw and cycloid states in Fig. 4 and Fig. S7 [23]. Here, τ is taken to be 0.1 ps, which is conservative and experimentally comparable. Its specific value does not affect the main conclusion of the current work. For the proper screw spin structure, its NSC flowing along x , constrained by $\mathcal{C}_{2x}\mathcal{T}$. One sees that the magnitude value of the $\sigma_{\text{prop}}^{xxx}$ reaches $20 \mu\text{A}/\text{V}^2$ (photon energy of 1–1.5 eV, in the mid-infrared frequency regime), if we take an effective thickness of monolayer NiI_2 to be 3 Å. This indicates that under a moderate light intensity e.g., 1 V/nm, one could achieve 6 μA photocurrent in the sample (with a typical lateral size of ~ 1 nm). Note that this current only arises when the spin spiral emerges, and it depends on the spiral patterns. Compared with the NSC values in nonmagnetic polar systems [46,47], this is large enough to be observed. The MIC only flows along y , and its x -flowing components diminish under $\mathcal{C}_{2x}\mathcal{T}$.

As for the cycloid spiral state, the NSC is unidirectionally along y [Fig. 4(b)]. The $\sigma_{\text{cyc}}^{yyy}$ value is approaching $50 \mu\text{A}/\text{V}^2$, at $\omega = 1.3$ eV. Similarly, the $\sigma_{\text{cyc}}^{yxx}$ can also reach $40 \mu\text{A}/\text{V}^2$, when $\omega = 1.7$ eV. We calculate the reversal of spin spiral chirality (between left-handed and right-handed), which corresponds to flip of \mathbf{q} . The BPV components also change their signs, consistent with previous

discussions. If we artificially “add” the \mathbf{q} and $-\mathbf{q}$ responses together, it gives zero BPV current, which agree with the vanishing BPV in the $\mathbf{q} = 0$ pattern (collinear ferromagnetic).

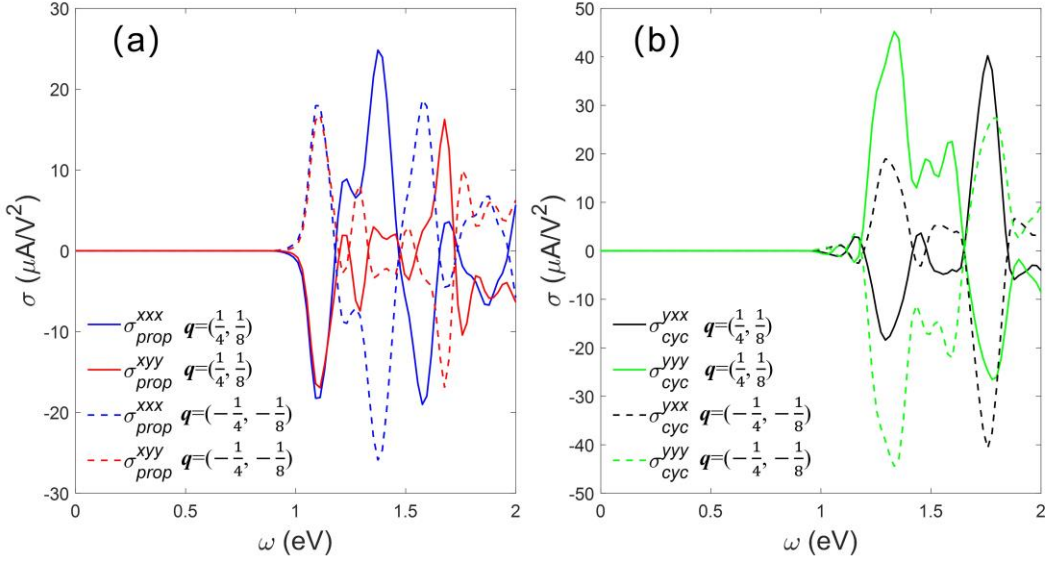


FIG. 4. NSC photoconductances for the monolayer NiI_2 under (a) proper screw and (b) cycloid spiral states, calculated by DFT with $\mathbf{q} = \left(\pm\frac{1}{4}, \pm\frac{1}{8}\right)$.

In summary, we systematically investigate the BPV responses under helimagnetic pattern, which exists in intrinsic multiferroic materials and can be generated through magnon excitation in collinear magnets. We illustrate our approach in a crystalline centrosymmetric lattice, and our tight-binding model and first-principles calculations suggest that spin spiral would effectively break \mathcal{P} , yielding distinct BPV photocurrents. We further use a realistic helimagnetic material, monolayer NiI_2 , to illustrate this process as an exemplary platform. We note that its potential multiferroic nature has been still under extensive investigation through different experimental efforts based on spin-resolved scanning tunneling microscope, the second harmonic generation, or linear dichroism. We propose that the direction-dependent BPV generation could serve as a supplementary technique to identify its symmetry.

Acknowledgments. We acknowledge the financial support from the National Natural Science Foundation of China (NSFC) under Grant Nos. 12274342, 12374065, and 12004306. Additionally, the authors acknowledge support from Bianshui Riverside Supercomputing Center (BRSC) and Beijing PARATERA Technology Co., LTD for providing high-performance resources for contributing to the research results reported within this paper.

References

[1] V. Belinicher, E. Ivchenko, and B. Sturman, *Kinetic theory of the displacement photovoltaic effect in piezoelectrics* *Zh Eksp Teor Fiz* **83**, 649 (1982).

[2] N. Kristoffel, R. Von Baltz, and D. Hornung, *On the intrinsic bulk photovoltaic effect: Performing the sum over intermediate states* Zeitschrift für Physik B Condensed Matter **47**, 293 (1982).

[3] J. Sipe and A. Shkrebtii, *Second-order optical response in semiconductors* Physical Review B **61**, 5337 (2000).

[4] R. von Baltz and W. Kraut, *Theory of the bulk photovoltaic effect in pure crystals* Physical Review B **23**, 5590 (1981).

[5] H. Wang and X. Qian, *Electrically and magnetically switchable nonlinear photocurrent in PT-symmetric magnetic topological quantum materials* npj Computational Materials **6**, 199 (2020).

[6] H. Pi, S. Zhang, and H. Weng, *Magnetic bulk photovoltaic effect as a probe of magnetic structures of $EuSn_2As_2$* Quantum Frontiers **2**, 6 (2023).

[7] Y. Zhang, T. Holder, H. Ishizuka, F. de Juan, N. Nagaosa, C. Felser, and B. Yan, *Switchable magnetic bulk photovoltaic effect in the two-dimensional magnet CrI_3* Nature Communications **10**, 3783 (2019).

[8] R. Fei, W. Song, L. Pusey-Nazzaro, and L. Yang, *P T-Symmetry-Enabled Spin Circular Photogalvanic Effect in Antiferromagnetic Insulators* Physical Review Letters **127**, 207402 (2021).

[9] Q. Xue, X. Mu, Y. Sun, and J. Zhou, *Valley contrasting bulk photovoltaic effect in a PT-symmetric $MnPSe_3$ monolayer* Physical Review B **107**, 245404 (2023).

[10] L. Liu, W. Liu, B. Cheng, B. Cui, and J. Hu, *Switchable Giant Bulk Photocurrents and Photo-spin-currents in Monolayer PT-Symmetric Antiferromagnet $MnPSe_3$* The Journal of Physical Chemistry Letters **14**, 370 (2023).

[11] R. Fei, W. Song, and L. Yang, *Giant photogalvanic effect and second-harmonic generation in magnetic axion insulators* Physical Review B **102**, 035440 (2020).

[12] H. Watanabe and Y. Yanase, *Photocurrent response in parity-time symmetric current-ordered states* Physical Review B **104**, 024416 (2021).

[13] H. Chen, M. Ye, N. Zou, B.-L. Gu, Y. Xu, and W. Duan, *Basic formulation and first-principles implementation of nonlinear magneto-optical effects* Physical Review B **105**, 075123 (2022).

[14] L. Z. Tan and A. M. Rappe, *Enhancement of the bulk photovoltaic effect in topological insulators* Physical Review Letters **116**, 237402 (2016).

[15] X. Jiang, L. Kang, J. Wang, and B. Huang, *Giant Bulk Electrophotovoltaic Effect in Heteronodal-Line Systems* Physical Review Letters **130**, 256902 (2023).

[16] H. Fu, K. Huang, K. Watanabe, T. Taniguchi, and J. Zhu, *Gapless spin wave transport through a quantum canted antiferromagnet* Physical Review X **11**, 021012 (2021).

[17] T. Kurumaji, S. Seki, S. Ishiwata, H. Murakawa, Y. Kaneko, and Y. Tokura, *Magnetoelectric responses induced by domain rearrangement and spin structural change in triangular-lattice helimagnets NiI_2 and CoI_2* Physical Review B **87**, 014429 (2013).

[18] X. Li, C. Xu, B. Liu, X. Li, L. Bellaiche, and H. Xiang, *Realistic Spin Model for Multiferroic NiI_2* Physical Review Letters **131**, 036701 (2023).

[19] J. Ni, X. Li, D. Amoroso, X. He, J. Feng, E. Kan, S. Picozzi, and H. Xiang, *Giant biquadratic exchange in 2D magnets and its role in stabilizing ferromagnetism of $NiCl_2$ monolayers* Physical Review Letters **127**, 247204 (2021).

[20] S. Son *et al.*, *Multiferroic-Enabled Magnetic-Excitons in 2D Quantum-Entangled Van der Waals Antiferromagnet NiI_2* Advanced Materials **34**, 2109144 (2022).

[21] T. Kurumaji, S. Seki, S. Ishiwata, H. Murakawa, Y. Tokunaga, Y. Kaneko, and Y. Tokura, *Magnetic-field induced competition of two multiferroic orders in a triangular-lattice helimagnet MnI_2* Physical Review Letters **106**, 167206 (2011).

[22] Y. Tokunaga, D. Okuyama, T. Kurumaji, T. Arima, H. Nakao, Y. Murakami, Y. Taguchi, and Y.

Tokura, *Multiferroicity in NiBr₂ with long-wavelength cycloidal spin structure on a triangular lattice* Physical Review B **84**, 060406 (2011).

[23] See Supplemental Material at <http://link.aps.org/supplemental/>.....Symmetry transformations of spin vector in the spherical coordinate; The MIC conductivity, NSC conductivities of $\pm q$ in the triangular lattice for proper screw spin spiral state with $q=(1/2,1/4)$; BPV effect in the triangular lattice with $q=(1/4,1/8)$; BPV effect in NiI₂ monolayer; Computational details. It includes references [7], [24-33].

[24] G. Kresse and J. Hafner, *Ab initio molecular dynamics for liquid metals* Physical Review B **47**, 558 (1993).

[25] G. Kresse and J. Furthmüller, *Efficient iterative schemes for ab initio total-energy calculations using a plane-wave basis set* Physical Review B **54**, 11169 (1996).

[26] P. E. Blöchl, *Projector augmented-wave method* Physical Review B **50**, 17953 (1994).

[27] J. P. Perdew, K. Burke, and M. Ernzerhof, *Generalized gradient approximation made simple* Physical Review Letters **77**, 3865 (1996).

[28] S. Grimme, *Semiempirical GGA-type density functional constructed with a long-range dispersion correction* Journal of Computational Chemistry **27**, 1787 (2006).

[29] A. A. Mostofi, J. R. Yates, G. Pizzi, Y.-S. Lee, I. Souza, D. Vanderbilt, and N. Marzari, *An updated version of wannier90: A tool for obtaining maximally-localised Wannier functions* Computer Physics Communications **185**, 2309 (2014).

[30] A. A. Mostofi, J. R. Yates, Y.-S. Lee, I. Souza, D. Vanderbilt, and N. Marzari, *wannier90: A tool for obtaining maximally-localised Wannier functions* Computer Physics Communications **178**, 685 (2008).

[31] Z. Dai, A. M. Schankler, L. Gao, L. Z. Tan, and A. M. Rappe, *Phonon-assisted ballistic current from first-principles calculations* Physical Review Letters **126**, 177403 (2021).

[32] X. Zhou, H. Van Driel, and G. Mak, *Femtosecond kinetics of photoexcited carriers in germanium* Physical Review B **50**, 5226 (1994).

[33] J. Sjakste, K. Tanimura, G. Barbarino, L. Perfetti, and N. Vast, *Hot electron relaxation dynamics in semiconductors: assessing the strength of the electron–phonon coupling from the theoretical and experimental viewpoints* Journal of Physics: Condensed Matter **30**, 353001 (2018).

[34] X. Mu, Y. Pan, and J. Zhou, *Pure bulk orbital and spin photocurrent in two-dimensional ferroelectric materials* npj Computational Materials **7**, 1 (2021).

[35] S. Kuindersma, J. Sanchez, and C. Haas, *Magnetic and structural investigations on NiI₂ and CoI₂* Physica B+C **111**, 231 (1981).

[36] Q. Song *et al.*, *Evidence for a single-layer van der Waals multiferroic* Nature **602**, 601 (2022).

[37] H. Ju *et al.*, *Possible persistence of multiferroic order down to bilayer limit of van der Waals material NiI₂* Nano Letters **21**, 5126 (2021).

[38] N. Liu, C. Wang, C. Yan, J. Hu, Y. Zhang, and W. Ji, *Varied competition among three multiferroic phases of NiI₂ from the bulk to the monolayer limit* arXiv preprint arXiv:2211.14423 (2022).

[39] M. Amini, A. O. Fumega, H. González-Herrero, V. Vaño, S. Kezilebieke, J. L. Lado, and P. Liljeroth, *Atomic-scale visualization of multiferroicity in monolayer NiI₂* arXiv preprint arXiv:2309.11217 (2023).

[40] Y. Tokunaga, D. Okuyama, T. Kurumaji, T. Arima, H. Nakao, Y. Murakami, Y. Taguchi, and Y. Tokura, *Multiferroicity in NiBr₂ with long-wavelength cycloidal spin structure on a triangular lattice* Physical Review B **84**, 060406 (2011).

[41] A. O. Fumega and J. Lado, *Microscopic origin of multiferroic order in monolayer NiI₂* 2D Materials **9**, 025010 (2022).

[42] Y. Jiang, Y. Wu, J. Zhang, J. Wei, B. Peng, and C.-W. Qiu, *Dilemma in optical identification of single-layer multiferroics* *Nature* **619**, E40 (2023).

[43] S. Wu, X. Chen, C. Hong, X. Hou, Z. Wang, Z. Sheng, Z. Sun, Y. Guo, and S. Wu, *Layer thickness crossover of type-II multiferroic magnetism in NiI₂* arXiv preprint arXiv:2307.10686 (2023).

[44] X.-s. Ni, D.-X. Yao, and K. Cao, *In-plane strain tuning multiferroicity in monolayer van der Waals NiI₂* arXiv preprint arXiv:2209.12392 (2022).

[45] D. Amoroso, P. Barone, and S. Picozzi, *Spontaneous skyrmionic lattice from anisotropic symmetric exchange in a Ni-halide monolayer* *Nature communications* **11**, 5784 (2020).

[46] A. M. Schankler, L. Gao, and A. M. Rappe, *Large Bulk Piezophotovoltaic Effect of Monolayer 2 H-MoS₂* *The Journal of Physical Chemistry Letters* **12**, 1244 (2021).

[47] C. Zhang, H. Pi, L. Zhou, S. Li, J. Zhou, A. Du, and H. Weng, *Switchable topological phase transition and nonlinear optical properties in a ReC₂H monolayer* *Physical Review B* **105**, 245108 (2022).